Lab Notes

Editors

Thomas M. Moses | Shane F. McClure
Sally Eaton-Magaña | Artitaya Homkrajae

Bicolor CHRYSOBERYL with Chrysoberyl and Alexandrite Zones

Recently, the Tokyo laboratory received for identification service a bicolor 0.73 ct octagonal step cut measuring 5.33 × 4.37 × 2.74 mm. One zone was greenish yellow, and the other was blue-green in fluorescent light and red-purple in incandescent light (figure 1).

Standard gemological testing results, including a refractive index of 1.747 to 1.753, and Raman spectroscopy proved that this stone was zoned chrysoberyl, and more notably an extremely rare zoned chrysoberyl and alexandrite gem. Microscopic examination revealed the presence of fingerprints, straight graining, and two-phase fluid inclusions (figure 2). No evidence of coating or clarity enhancement was observed. This is the first time GIA has documented a stone composed of chrysoberyl and alexandrite.

Hikaru Sato

Figure 1. This 0.73 ct octagonal step cut was composed of chrysoberyl and alexandrite. The alexandrite portion showed a color change from blue-green in fluorescent light to red-purple in incandescent light.

Large Natural DIAMONDS with Asteriated Cloud Inclusions

The Carlsbad laboratory recently received for scientific examination two natural diamonds that displayed remarkable light brown cloud inclusions resembling stars (figure 3, left). Such diamonds are sometimes referred to as "asteriated" or "star" diamonds in the literature. Clouds are found in sectors correlating with high hydrogen and nickel concentrations and are thought to consist of graphite inclusions (B. Rondeau et al., "Three historical 'asteriated' hydrogen-rich diamonds: Growth history and sector-dependent

Figure 2. Two-phase fluid inclusions in the bicolor chrysoberyl; field of view 2.00 mm.

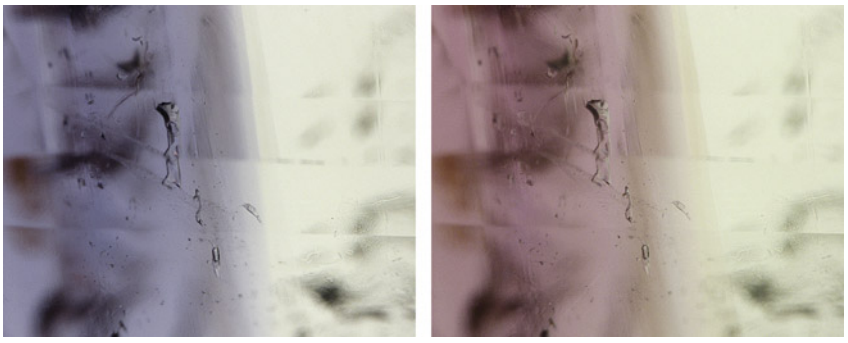

Editors' note: All items were written by staff members of GIA laboratories.

GEMS & GEMOLOGY, Vol. 60, No. 2, pp. 212–225.

Figure 3. Left: An 8.14 ct and an 8.57 ct diamond containing brown asteriated cloud inclusions with sixfold symmetry. Right: The clouds fluoresced green when exposed to long-wave UV. The purple reflections of the UV source are likely caused by surface imperfections on the rough surface.

impurity incorporation," *Diamond and Related Materials*, Vol. 13, No. 9, 2004, pp. 1658–1673; A.R. Lang et al., "Is dispersed nickel in natural diamonds associated with cuboid growth sectors in diamonds that exhibit a history of mixed-habit growth?" *Journal of Crystal Growth*, Vol. 263, No. 1-4, 2004, pp. 575–589; K.V. Smit et al., "Diamond growth from C-H-N-O recycled fluids in the lithosphere: Evidence from CH_4 micro-inclusions and $\delta^{13}C$-$\delta^{15}N$-N content in Marange mixed-habit diamonds," *Lithos*, Vol. 265, 2016, pp. 68–81).

While asteriated diamonds are occasionally submitted to GIA (Fall 2019 Lab Notes, p. 417; Fall 2019 Gem News International, p. 443), the two recently examined stones were particularly notable for their large size and preserved natural forms. The 8.14 ct diamond was resorbed and maintained most of its rough form on one side, and it was sliced to reveal the underlying inclusion pattern on the other. The preserved rough surfaces also displayed brown radiation stains, indicating their past history of natural alpha irradiation followed by annealing in the earth. The 8.57 ct diamond was a polished stone with bruted edges. In both stones, and consistent with similar asteriated diamonds previously studied, the clouds fluoresced green when subjected to long-wave UV (figure 3, right).

Both diamonds had high hydrogen concentrations, as detected by bulk Fourier-transform infrared spectroscopy. Photoluminescence (PL) mapping using 455 nm laser excitation showed a prominent wide S3 center (496.7 nm), correlating directly with the green fluorescing clouds (figure 4). This peak is associated with nickel (A.M. Zaitsev, *Optical Properties of Diamond: A Data Handbook*, Springer-Verlag, Berlin, 2001). Other nickel-related peaks in the cloud region were detected in both stones via 633 nm laser excitation at 694.2, 700.5, 787.3, and 793.4 nm (figure 5). Unattributed peaks at 709.1 and 729.6 nm were also detected. Higher peak intensities at 793.5 and 801.8 nm in the cloud inclusion sectors were revealed using 785 nm laser excitation. The former peak is associated with the S2 and S3 centers (Zaitsev, 2001), and the latter is potentially NE8, a nickel-nitrogen complex center (T. Gaebel, "Stable

Figure 4. A: The 8.14 ct diamond maintained much of its textured rough surface on one side and had a sliced surface to reveal the underlying cloud. B: The cloud fluoresced green when exposed to long-wave UV, correlating to the peak area intensity of the S3 center; field of view 7.19 mm. C: The false-color heat map showing the peak area intensity of the S3 center was collected using 455 nm laser excitation and included 43,976 spectra.

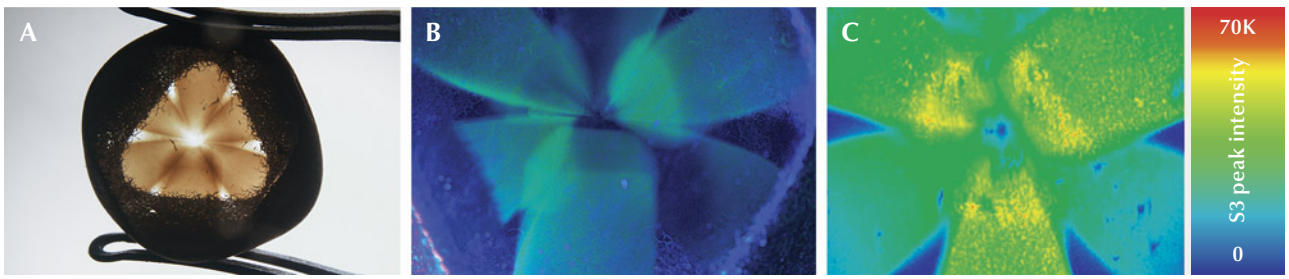

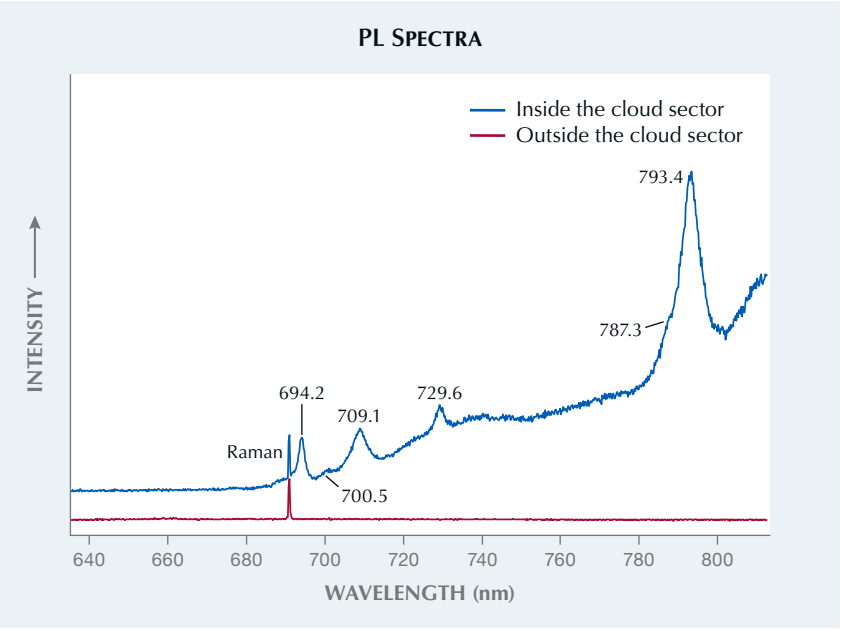

Figure 5. PL spectra for the 8.14 ct diamond when mapped with 633 nm laser excitation. Several nickel-related defects were detected inside the cloud inclusion sector but not outside of it. The spectra are stacked for clarity, and the Raman peaks are scaled as equal.

single-proton source in the near infrared," *New Journal of Physics*, Vol. 6, 2004, article no. 98).

Both diamonds were analyzed by X-ray computed microtomography (µ-CT), in which the asteriated growth sectors, ~{100}, were visible in three-dimensional reconstructions (figure 6; see video at https://www.gia.edu/gems-gemology/summer-2024-lab-notes-diamonds-asteriated-cloud-inclusions). The contrast in the µ-CT reconstruction should be mainly a function of the mean atomic number of the material. The asteriated regions more strongly absorb X-rays than the rest of the diamond, an indication that the combined signal from the diamond and inclusions likely had a higher atomic number.

These aesthetically pleasing and scientifically interesting diamonds provide stunning examples of what the natural world has to offer.

Taryn Linzmeyer, Henry Towbin, and Sally Eaton-Magaña

Figure 6. Left: µ-CT cross section of the 8.57 ct diamond. Asteriated growth sectors are observed following the <100> crystallographic directions. While the cloud sectors appear solid, they are actually composed of microscopic inclusions. Right: 3D rendering of the segmented µ-CT image highlighting the asteriated sectors in yellow within the semi-transparent diamond.

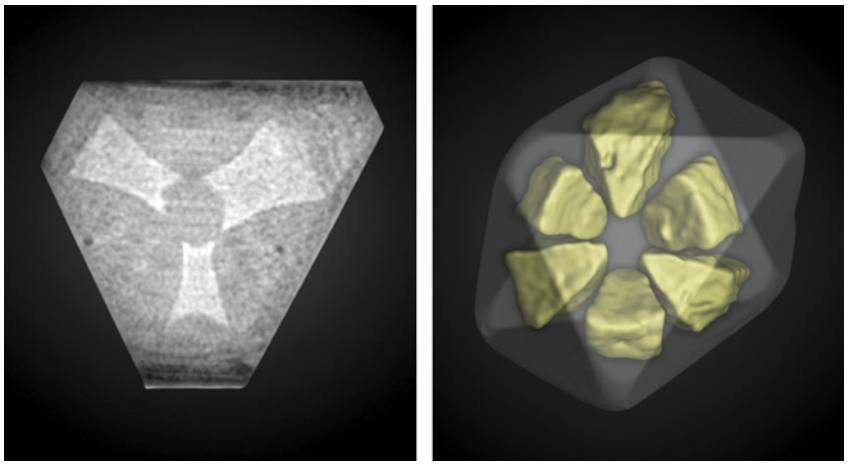

Cat's-Eye HEXAGONITE

A 0.50 ct purplish pink cabochon displaying chatoyancy (figure 7) was recently submitted to the New York laboratory as a ruby. Standard gemological testing revealed a spot refractive index of 1.63 and a hydrostatic specific gravity of 3.02, neither of which were consistent with the expected values for corundum. Raman analysis, along with the specific gravity and refractive index, confirmed the identity of this mineral as tremolite (figure 8).

Hexagonite, a variety of tremolite, ranges in color from red to pink to purple. Initially believed to be a hexagonal form of tremolite, and named

Figure 7. This 0.50 ct purplish pink cabochon is a rare chatoyant example of hexagonite.

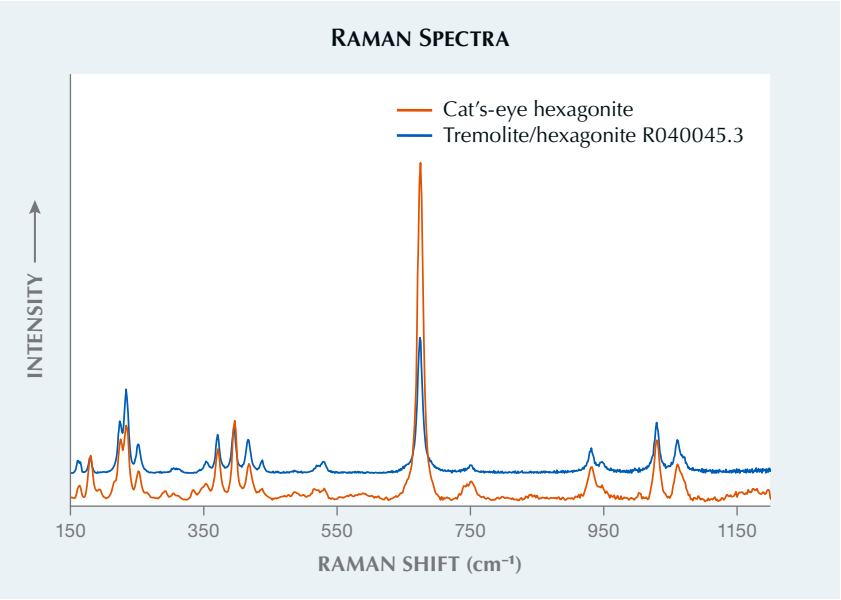

Figure 8. Raman spectrum of the cat's-eye hexagonite compared to a known tremolite reference spectrum. Spectra are offset vertically for clarity.

accordingly, the mineral was later confirmed to be monoclinic (Summer 1985 Lab Notes, p. 110). This mineral can be found in facetable sizes in St. Lawrence County and Lewis County, both in the state of New York. Though typically under a carat and heavily included, a few large transparent stones have been unearthed.

Under magnification, the densely included stone displayed long silk and needles (figure 9). These inclusions, when oriented parallel to each other and the base of a cabochon, create the cat's-eye phenomenon.

Courtney Robb

Metallic See-Through Backing on Omphacite JADE

The Carlsbad laboratory recently received for identification an omphacite jade carving in the shape of a pea pod (figure 10) with an unusual effect created by its backing. Adhered on the back of the carving, which measured 23.71 × 9.67 × 2.59 mm and weighed 4.52 ct, was a thin layer of plastic-like material with a metallic luster. Standard gemological testing revealed a spot refractive index of 1.66 and weak blue fluorescence due to the plastic layer; microscopic observation showed the film in reflected light. A metallic film of 0.10 mm thickness was found to be adhered on the back of the piece to create a metallic look. It had a see-through quality, shown in figure 11. Raman analysis of the thin film closely matched with a plastic used in Mylar.

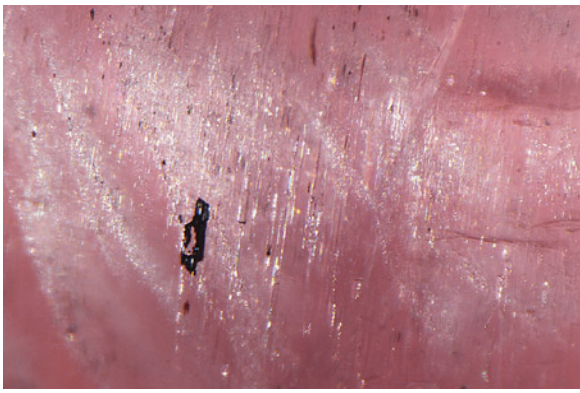

Figure 9. Light reflects off densely packed silk, needles, and particles to create the cat's-eye effect. Field of view 1.31 mm.

Figure 10. A: Face-up view of the 23.71 × 9.67 × 2.59 mm jade carving. B: The profile view shows the thickness of the thin film lining. C: The back of the carving shows the reflective metallic luster of the film.

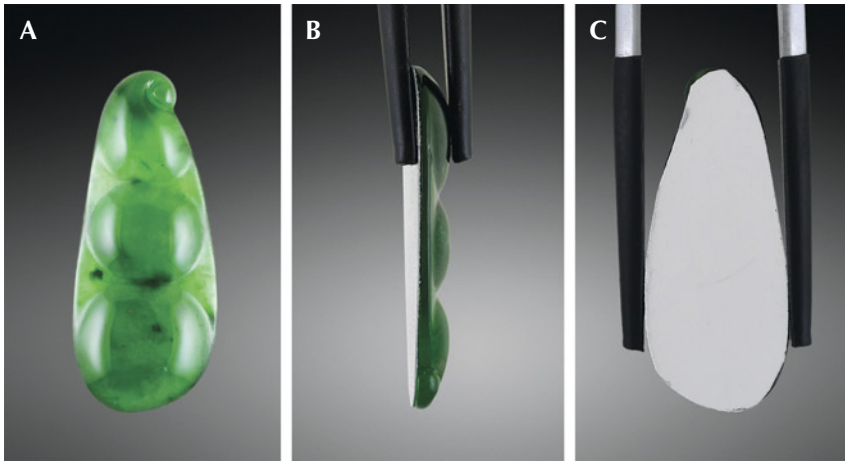

Figure 11. The see-through nature of the carving and thin reflective film backing.

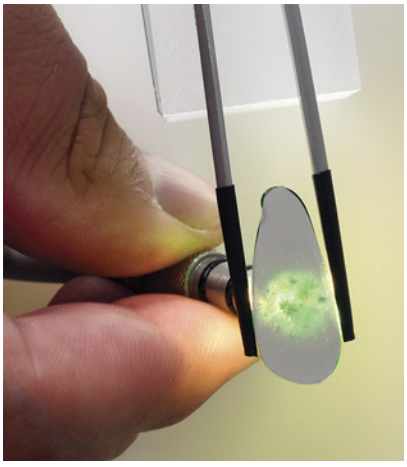

Figure 12. The five CVD-grown diamond samples set in variously designed metal rings: ~5.00 ct orange heart brilliant (A), ~5.58 ct greenish blue pear brilliant (B), ~2.30 ct greenish blue cushion modified brilliant (C), ~1.65 ct yellowish orange square emerald cut (D), and ~3.08 ct grayish green emerald cut (E).

Analysis for polymer impregnation with Fourier-transform infrared spectroscopy revealed the importance of direction in testing the piece. If the laser was positioned perpendicular to the metallic film so that the laser went through the film, the glue layer would be detected, creating a false positive for polymer impregnation. Analysis parallel to the metallic film proved the piece was not polymer impregnated. Understanding and identifying all components of such a piece is very important in the determination of jade treatment types.

Maxwell Hain

Large Treated-Color CVD LABORATORY-GROWN DIAMOND Rings

Laboratory-grown diamonds have become a prominent sector of the jewelry market. Part of the consumer appeal relates to the availability of stones with vibrant colors and the range of carat sizes. The New York laboratory received one submission of five laboratory-grown diamonds produced by chemical vapor deposition (CVD) set in variously designed metal rings (figure 12). These samples represent the wide range of stone colors and sizes created using CVD growth technology. CVD diamonds commonly undergo post-growth treatments to improve clarity and color. Post-growth treatments such as high-pressure, high-temperature (HPHT) processing, irradiation, and annealing are often necessary for a more desirable color result. High-temperature treatment may remove internal synthetic graining patterns to improve clarity. Gemologists identify the treatments based on subtle indicators using several methods, specifically spectroscopic data analysis.

Infrared absorption spectroscopy showed no absorption related to nitrogen or boron, classifying these CVD diamonds as type IIa. The visible/near-infrared absorption spectrum, taken at room temperature, displayed GR1 absorption in all five samples (e.g., figure 13). Photoluminescence spectroscopy revealed a GR1 emission and silicon-vacancy doublet at 736.6 and 736.9 nm in samples B–E. The SiV^- doublet is usually indicative of CVD growth since it is rarely seen in natural diamonds or HPHT-grown diamonds. The presence of the SiV^- reveals CVD growth but does not contribute to the color within these stones. The GR1 defect in these CVD diamonds is evidence of post-growth treatment that included irradiation causing alterations in bodycolor.

The data suggest the samples underwent various treatments including HPHT annealing, irradiation, and possible post-irradiation annealing. Based on spectroscopic data, sample A shows evidence of HPHT treat-

Figure 13. Four of the five CVD diamond samples are shown with a clear GR1 defect. Spectra are offset vertically for clarity.

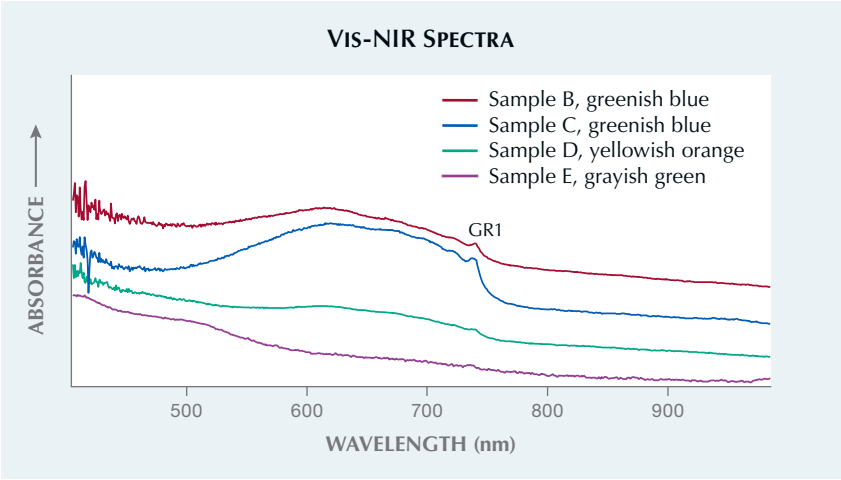

ment due to the lack of the 468 nm peak, irradiation, and low-temperature annealing to create the orange color. The greenish blue colors for samples B and C were created with irradiation and possibly annealing. Both samples contained strong absorption from the GR1 center and a weak 666.5 nm peak that can be annealed out at temperatures ranging from 420° to 540°C (see A.T. Collins, "Spectroscopy of defects and transition metals in diamond," *Diamond and Related Materials*, Vol. 9, Nos. 3–6, 2000, pp. 417–423). Sample D likely underwent irradiation and subsequent low-temperature treatment to create the yellowish orange color. The grayish green color in sample E was likely the result of HPHT treatment and irradiation with subsequent annealing. We consider the annealing temperatures to be low to moderate because of the lighter color result in sample E.

Gemological and spectroscopic analysis revealed that all five samples were type IIa CVD-grown diamonds that underwent post-growth treatment to achieve fancy colors. The laboratory-grown diamond market continues to develop, driven by consumer demand for these affordable mined diamond alternatives.

Stephanie Persaud and Erica Watts

Figure 14. The white saltwater nacreous pearl weighing 1.90 ct and measuring 6.75 × 6.55 × 6.19 mm.

PEARLS

Seed Features in an Akoya Keshi Pearl

Recently, GIA's Mumbai laboratory received a white button-shaped saltwater nacreous pearl weighing 1.90 ct and measuring 6.75 × 6.55 × 6.19 mm for pearl identification (figure 14). When observed under high magnification, the pearl's surface showed fine fingerprint-like overlapping platelets typical of aragonite. Energy-dispersive X-ray fluorescence revealed a manganese level below the detection limit and a strontium level of 857 ppm, confirming the pearl's saltwater origin. Under long-wave ultraviolet light, the pearl exhibited a moderate greenish yellow reaction, which is typical for pearls from the *Pinctada* species.

Real-time X-ray microradiography (RTX) analysis revealed a small oval-shaped core surrounded by a dark gray organic-rich concentric structure displaying an acicular (or radial) pattern

Figure 15. A: RTX image showing an oval core in an organic-rich concentric structure surrounded by an acicular pattern. An elongated, irregular Tokki-like feature with a linear structure is positioned on the top of the concentric growth structure. B: µ-CT image showing the oval core with a seed feature on the inner growth arc. C: µ-CT image showing another seed feature on the outer growth arc.

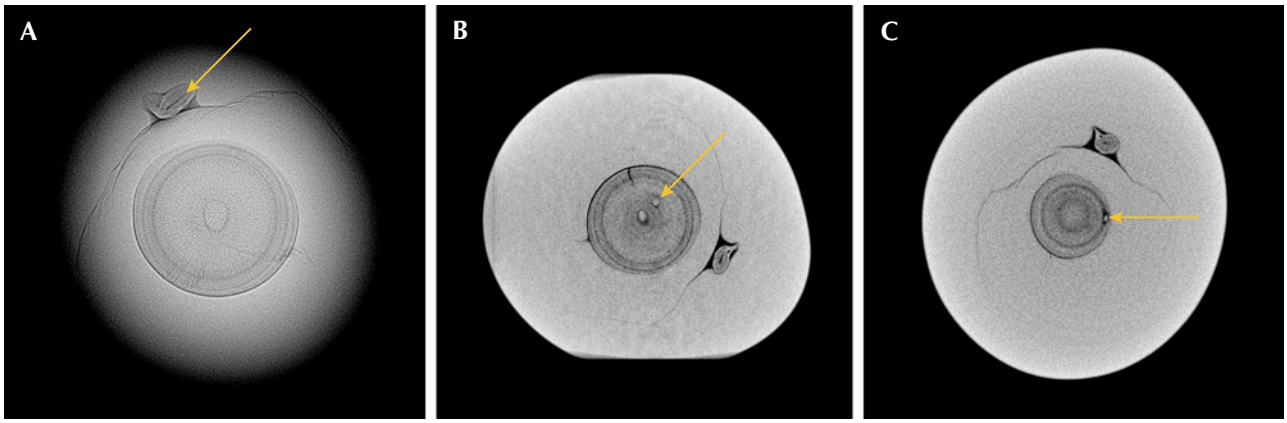

(figure 15A). An additional elongated, irregular feature with a linear structure at its center was positioned above the central structure, as indicated by the arrow in figure 15A. The growth characteristic of this additional feature looked similar to the internal structure of surface protuberances that sometimes form on bead cultured pearls. Bead cultured pearls with additional surface protuberances are sometimes referred to as Tokki pearls (M.S. Krzemnicki et al., "Tokki pearls: Additional cultured pearls formed during pearl cultivation: External and internal structures," *32nd International Gemmological Conference*, 2011; https://www.ssef.ch/wp-content/uploads/2018/01/SSEF_Tokki_pearls.pdf). Owing to the existence of an elongated feature, it was questionable whether this was a non-bead cultured (NBC) pearl.

Further examination using X-ray computed microtomography (µ-CT) revealed two light gray seed features in the main concentric growth structure: a larger one near the core in the acicular area and a smaller one close to the outline of the concentric growth structure (figure 15, B and C). Previous studies of saltwater NBC pearls, known as keshi cultured pearls, produced from various *Pinctada* mollusk species have shown that NBC pearls with organic-rich concentric growth structures sometimes contain seed features made up of a calcium carbonate substance; these seed features appeared light gray in microradiographs. The seed features can be different sizes and shapes, and they are typically found within organic-rich areas in loose concentric ring structures (A. Homkrajae et al., "Internal structures of known *Pinctada maxima* pearls: Cultured pearls from operated marine mollusks," Fall 2021 *G&G*, pp. 186–205).

Conversely, organic-rich concentric structures with acicular patterns are typically associated with calcite formation in some natural pearls. It is therefore unusual to observe seed features in an acicular organic-rich structure. The presence of both seed features and the elongated Tokki-like feature in this pearl indicated an NBC pearl formation, most likely produced from the *Pinctada fucata* (akoya) oyster based on internal structure and external appearance.

While seed features can be found in natural pearls, they are usually located on the outer concentric rings closer to the pearl's surface and, in some cases, may contain fine growth arcs (A. Homkrajae et al., "Internal structures of known *Pinctada maxima* pearls: Natural pearls from wild marine mollusks," Spring 2021 *G&G*, pp. 2–21). In addition, they have a different radiopacity compared to their cultured counterparts.

Differentiating between natural and cultured pearls poses a significant challenge, given that pearls are unique products of living organisms. µ-CT has enabled gemologists to provide conclusive results on certain features associated more with NBC pearls that are not visible on RTX images, such as the seed features in this example. Seed features are more commonly observed in cultured pearls originating from *Pinctada maxima*. This pearl is noteworthy due to the rarity of seed features in akoya keshi pearls and in this case its combination with an acicular structure.

Jayesh Surve and Abeer Al-Alawi

A Large Multicolored Natural Blister Pearl

Pearls have always been renowned for their beauty and mystical allure. From the wide range of pearls examined in GIA's Mumbai laboratory, one recent submission was highlighted for its remarkable size and unique multicolored appearance. The baroque-shaped natural blister pearl weighed 90.08 ct and measured 28.66 × 22.19 × 18.50 mm (figure 16).

The surface exhibited an array of colors. The top was an attractive silvery white with strong orient, while the sides displayed various shades of red ranging from orangy red to dark red with a yellowish cream hue on the base. Under high magnification, a nacreous area with a fine platy structure was observed on the top, and a non-nacreous area on the side and base displayed a complex crystalline structure along with minor surface-reaching cracks (figure 17, A–C). When exposed to long-wave ultraviolet radiation, the red part of the pearl was inert, while the silvery white area emitted a moderate greenish yellow reaction, which is a common reaction for unprocessed and untreated pearls.

Energy-dispersive X-ray fluorescence spectrometry on multiple spots of the surface revealed a magnesium range from below detection limits up

Figure 16. The multicolored pearl weighing 90.08 ct and measuring 28.66 × 22.19 × 18.50 mm.

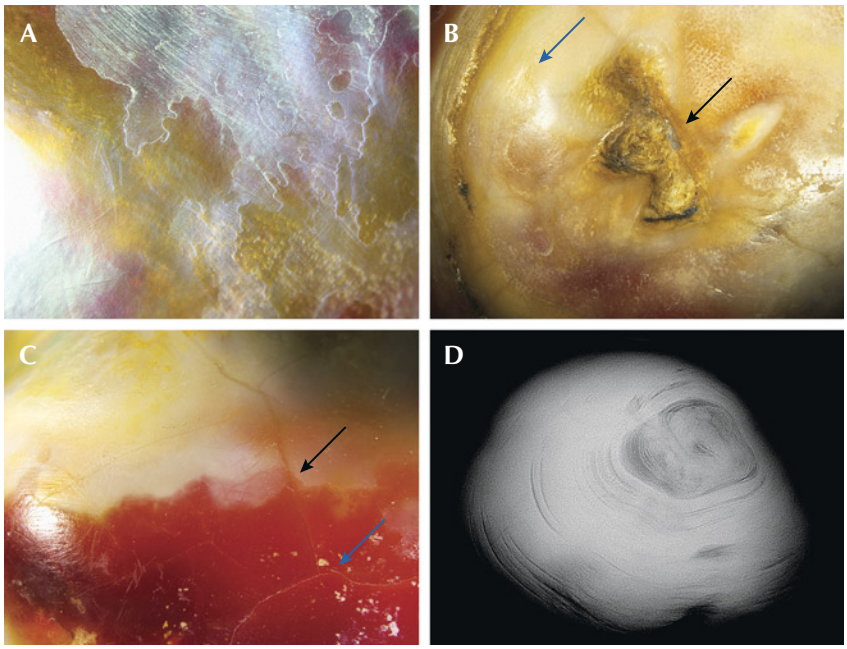

Figure 17. A: Nacreous platy structure on the top portion of the pearl. B: Nacreous structure (blue arrow) and non-nacreous structure (black arrow). C: Surface-reaching cracks (blue arrow) and boundary between two colored portions of the non-nacreous surface (black arrow). D: RTX image showing the organic-rich concentric natural growth pattern following the shape of the pearl. Fields of view: 0.80 mm (A), 2.20 mm (B), and 1.5 mm (C).

to 35 ppm and strontium levels ranging from 1031 to 2646 ppm, indicating a saltwater origin. Real-time X-ray microradiography (RTX) imaging showed an off-center organic-rich core surrounded by concentric growth arcs following the pearl's shape (figure 17D). This distinctive internal structure corresponded to those observed in natural whole pearls. However, the presence of a worked area on the base indicated the pearl had once been attached to a mollusk's shell. Therefore, it was identified as a natural blister pearl ("Natural shell blisters and blister pearls: What's the difference?" *GIA Research News*, August 26, 2019).

Raman analysis was conducted on two spots using an 830 nm laser excitation due to higher background fluorescence in this sample. The nacreous area showed peaks at 701, 704, and 1085 cm^{-1} indicative of aragonite, while the non-nacreous orangy red area revealed peaks at 283, 712, and 1085 cm^{-1} indicative of calcite (figure 18). Ultraviolet/visible reflectance spectra on the same spots showed reflectance minima at around 280 nm and an area of lower reflectance between 420 and 500 nm, similar to that observed in pearls from the *Pinctada maxima* mollusk.

Since no indication of color pigments was observed on the nacreous portion of the pearl, the various colors seen on the nacreous surface were likely due to the iridescent effect in the multilayered aragonite platelet structure, similar to abalone pearls. The cause of the red coloration on the non-nacreous area remains unclear; however, no indications of treatment were identified. According to previous studies on pen pearls (e.g., Fall 2009 Gem News International, pp. 221–223), red coloring in pen pearls is associated with carotenoid pigments, and porphyrins may be responsible for imparting a red color. However, the Raman peaks reported in those studies were not detected in this sample.

This large multicolored natural blister pearl with both nacreous and non-nacreous surfaces is an intriguing product of nature.

Anukul Belanke, Roxane Bhot Jain, and Abeer Al-Alawi

Figure 18. The Raman spectra showed peaks at 283 and 712 cm^{-1} indicative of calcite and typical aragonite features at 701, 704, and 1085 cm^{-1} at 830 nm excitation.

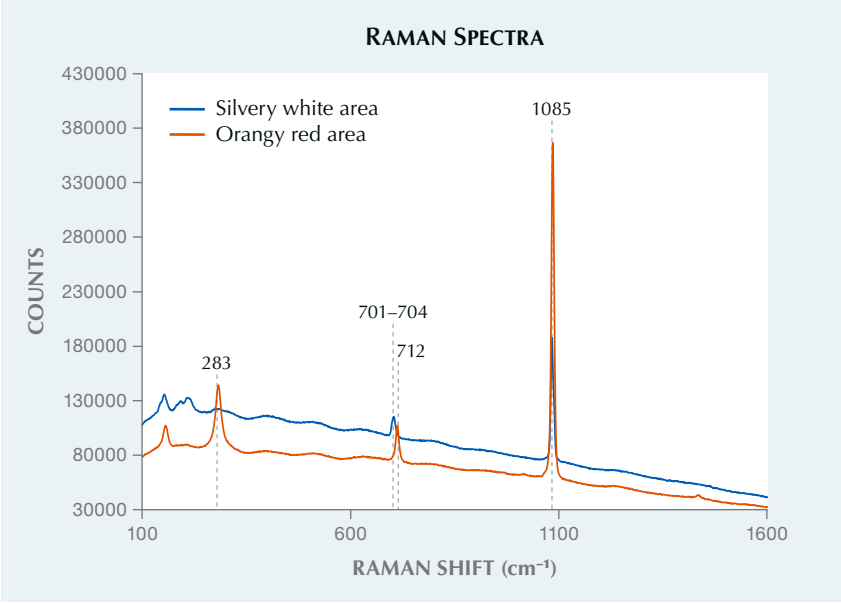

Figure 19. A white saltwater natural calcite pearl weighing approximately 0.12 ct and measuring 2.55 mm in diameter.

Calcite Pearl with Red X-Ray Fluorescence

GIA's Mumbai laboratory recently received for identification seven strands containing 1,170 variously shaped white to cream-colored pearls. Real-time X-ray microradiography (RTX) revealed that most of the pearls were of natural origin, and a few were non-bead cultured pearls. All the natural pearls showed an inert reaction when exposed to X-ray excitation due to their saltwater origin, except for one white near-round pearl that measured 2.55 mm in diameter and weighed approximately 0.12 ct (figure 19). The pearl exhibited a very unusual deep red fluorescence (figure 20, left).

RTX analysis showed a minimal growth structure with a few faint growth arcs in the outer area of the pearl and one distinct growth ring closer to the center near the drill hole (figure 21, left). X-ray computed microtomography (μ-CT) further revealed a very fine growth arc within the center ring (figure 21, right). These were consistent with structures observed in natural pearls from the *Pinctada* species.

Figure 20. Left: An X-ray fluorescence image of the pearl showing a deep red fluorescence. Right: This photomicrograph of the pearl's inner layer reveals a network of blue subsurface vein-like features; field of view 1 mm.

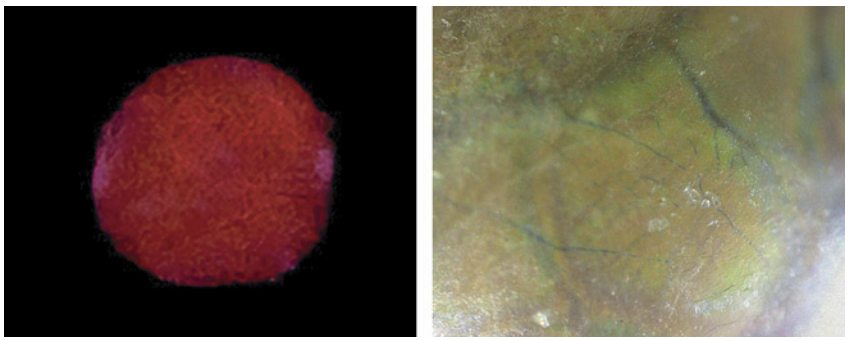

Externally, the pearl looked similar to the other pearls in the strands, possessing a medium surface luster with orient. Examination at high magnification exposed a translucent layer showing characteristic fingerprint-like overlapping surface platelets with blue subsurface vein-like features branching out in a dendritic pattern beneath it (figure 20, right). Interestingly, similar blue vein-like features have been observed in some research pearl samples reportedly produced from *Pinctada radiata* mollusks from the Persian (Arabian) Gulf. No visual indications of treatment on the surface were observed. Under long-wave ultraviolet light, the pearl exhibited a moderate chalky bluish green reaction. Energy-dispersive X-ray fluorescence revealed a manganese level of 76 ppm and a strontium level of 1599 ppm, characteristic of saltwater origin.

Raman analysis conducted on two randomly chosen spots using 514 nm laser excitation revealed peaks at 154, 282, 712, 1085, and 1437 cm^{-1}, indicating calcite composition. Saltwater calcite pearls with a "nacreous-looking" surface have been previously examined by GIA laboratories (Winter 2022 Lab Notes, pp. 477–478; Spring 2024 Lab Notes, pp. 69–71). However, they lacked visible fluorescence to X-ray excitation and exhibited a clear, evenly spaced fine concentric ring structure, contrasting with the minimal growth structure of this pearl.

Spectroscopic analysis combined with microscopic examination suggested that the red fluorescence was not a result of any surface treatment, but rather a natural phenomenon. Orange to red fluorescence has been previously recorded in freshwater pearls containing calcite and vaterite (both of which are polymorphs of calcium carbonate) when activated by cathodoluminescence or X-ray excitation. This luminescence has been associated with the presence of Mn^{2+} in either calcite or vaterite in freshwater non-bead cultured pearls from China (S. Karampelas et al., "Chemical characteristics of freshwater and saltwater natural and

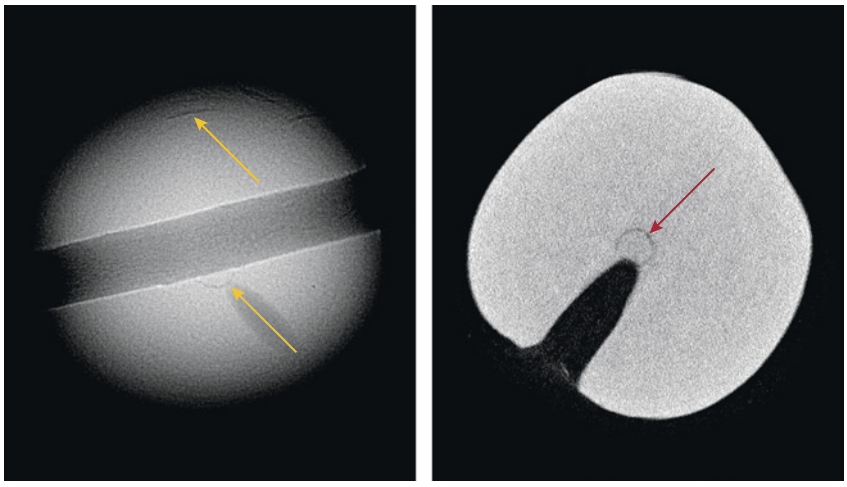

Figure 21. Left: RTX image displaying very fine growth arcs (yellow arrows). Right: µ-CT image showing a center ring with a very fine growth arc inside (red arrow).

cultured pearls from different bivalves," *Minerals*, Vol. 9, No. 6, 2019, article no. 357). Although such red fluorescence in saltwater pearls has not been previously recorded, we suspect a connection to the presence of calcite on the pearl's surface, though the existence of vaterite in the inner nacre layers remains a possibility.

Further research on the chemical composition of the surface and inner cross-sectional layers of this sample is required to understand the exact formation and the specific cause of this reaction in saltwater pearls. This is the first time GIA has encountered a nacreous-looking calcite pearl that exhibited red fluorescence when subjected to X-ray excitation.

Rajesh Patel and Abeer Al-Alawi

Large *Tridacna* Shell with a Blister Pearl and a Shell Blister

A collection of various shells was recently submitted to the Mumbai laboratory. Among these was a large shell from the *Tridacna* species, featuring an attached blister pearl and a shell blister (figure 22). The shell was sawn on three sides to create a stable base for display and weighed approximately 1.37 kg.

Externally, the off-white shell exhibited a wavy pattern of thin, sharp ridges in rows, along with several parasitic holes. Unlike shells from other mollusks, *Tridacna* shells exhibit thick growth layers of calcium carbonate in a rippling, overlapping pattern. In the thick cross section of this shell, the growth layers opened into a large cavity at one end, divided into two parts by a thin, wavy layer of calcium carbonate (figure 23A).

The interior surface was white to light cream in color, with a smooth porcelain-like surface featuring two protuberances that appeared to be a blister pearl and a shell blister, each naturally attached and displaying distinct striations toward their respective outer edges. The light gray blister pearl with brownish patches on its body, measuring approximately 37.31 × 25.42 mm, displayed a relatively smooth porcelaneous surface with a short and patchy flame-like structure (figure 23B). The dull cream-colored shell blister, measuring 28.93 × 16.63 mm, protruded outward and resembled a cone, with a concave opening at its apex encircled by a brown area rich in organic matter (figure 23C).

Figure 22. Tridacna *shell with a natural blister pearl measuring 37.31 × 25.42 mm (left) and a shell blister measuring 28.93 × 16.63 mm (right).*

Figure 23. A: Cross section of the shell in the cut area. B: The porcelain-like surface of the blister pearl was characterized by a short and patchy flame-like structure; field of view 16.3 mm. C: The concave opening encircled by a brown organic-rich area on the shell blister; field of view 16.3 mm.

Under long-wave ultraviolet radiation, the shell and shell blister exhibited a moderate to strong chalky blue reaction, while the blister pearl displayed reddish purple patches on its surface. Energy-dispersive X-ray fluorescence analysis could not be conducted due to the size of the specimen. Raman analysis of both the blister pearl and the shell blister showed a weak doublet at 701 and 704 cm^{-1} and a peak at 1086 cm^{-1}, indicative of aragonite, with no indication of color treatment.

The identity of both the blister pearl and the shell blister was confirmed by real-time X-ray microradiography (RTX) analysis. Both features exhibited cavity or void-like structures that have previously been observed in whole pearls and blister pearls from the *Tridacna* species (Summer 2017 Lab Notes, pp. 231–233). The blister pearl revealed a globule-like structure at its base, with a dark void of varying opacity and organic-rich material (figure 24, left). Its firm attachment to the shell was visible at one end, with discernible shades of gray indicating organic material, confirming its identity as a blister pearl. Conversely, the shell blister displayed a faint void lacking distinct features and contained light gray tubular features indicative of the parasitic boreholes and channels that contributed to its formation (figure 24, right). Parasite channels in the shell were displayed as dark gray lines in random patterns and different thicknesses.

Studies have shown that blister pearls develop as whole pearls within the mantle, normally appearing as tall domes fused with the shell, while shell blisters are caused by foreign bodies and appear as shallow bumps on the shell's inner surface ("Natural shell blisters and blister pearls: What's the difference?" *GIA Research News*, August 26, 2019). Differentiating between blister pearls and shell blisters can be challenging as they can have a similar surface appearance; thus, identification must be confirmed using internal growth structures. The presence of both within the submitted shell pro-

Figure 24. Left: RTX image of the larger blister pearl with a globule-like structure (indicated by the arrow) and a dark void following the shape of the pearl. Right: RTX image of the smaller shell blister with a faint void and white tubes (indicated by the arrow).

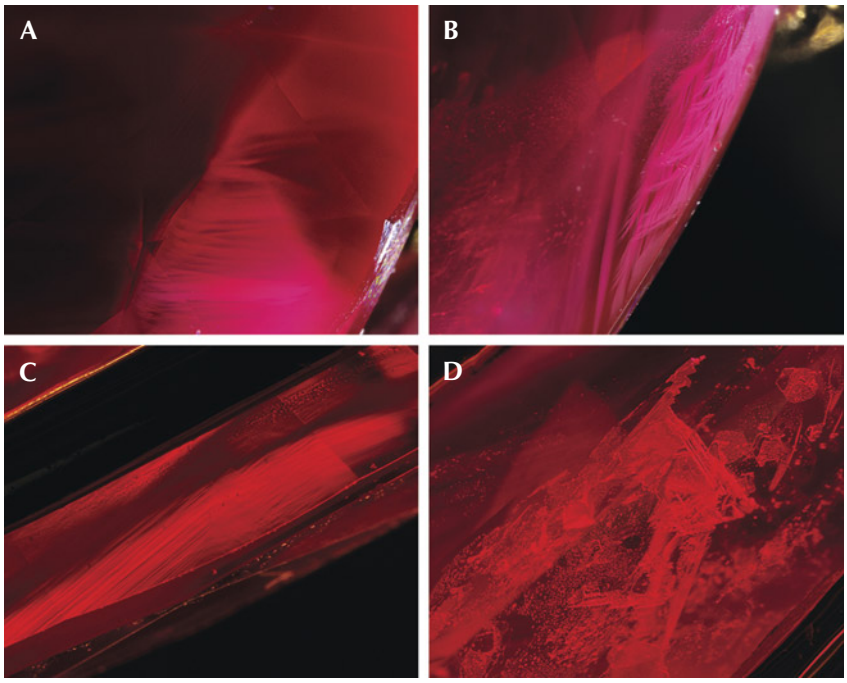

Figure 25. Inclusions in a Ramaura flux-grown synthetic ruby: angular milky clouds (A), wispy veil-like irregular hazy clouds (B), strong angular graining (C), and triangular flux inclusions (D). Fields of view 2.96 mm (A, B, and D) and 3.99 mm (C).

vided gemologists with valuable insights on their unique appearance and formation, offering significant gemological and scientific information for future reference.

Andrew Aron, Abeer Al-Alawi, and Roxane Bhot Jain

Natural-Looking Inclusions in a Ramaura SYNTHETIC RUBY

GIA's Tokyo laboratory recently observed a vivid red stone mounted in a ring that was submitted for an identification and origin report. This stone measured 14.13 × 5.41 × 3.60 mm, with an estimated weight around 2.14 ct. It showed two strong specific absorption lines around 468 and 476 nm in the blue area through a handheld spectroscope, and its gemological properties confirmed ruby.

The ruby fluoresced strong red to long- and short-wave ultraviolet light. It contained natural-looking angular milky clouds (figure 25A), unusual wispy veil-like milky clouds (figure 25B), strong angular graining (figure 25C), and triangular negative crystals containing flux-like materials and minute bubbles (figure 25D). Although the pattern of milky clouds gave the appearance of a natural origin, the wispy veil-like clouds and triangular flux-like inclusions are characteristics of flux-grown synthetic ruby.

Laser ablation–inductively coupled plasma–mass spectrometry (LA-ICP-MS) was used to determine the chemical nature of the stone. The analysis revealed lower concentrations of magnesium and gallium and much higher concentrations of lanthanum, platinum, and lead than those found in natural rubies (table 1). Vanadium was not detected. These chemical features, especially the absence of vanadium and the detection of lanthanum, platinum, and lead, were abnormal for natural ruby. The inclusions and trace element chemistry, particularly the presence of lanthanum, suggested a Ramaura flux-grown synthetic ruby (e.g., S. Muhlmeister et al., "Separating natural and synthetic rubies on the basis of trace-element chemistry," Summer 1998 *G&G*, pp. 80–101). The inclusions were consistent with those in Ramaura flux-grown rubies except for the presence of natural-looking milky clouds (R.E. Kane, "The Ramaura synthetic ruby," Fall 1983 *G&G*, pp. 130–148).

The Ramaura flux process, first reported in 1983, can produce red corundum by spontaneous nucleation of a crystal from a high-temperature flux. Ramaura synthetic rubies are formed using a flux of Bi_2O_3 and PbF_2

TABLE 1. Trace element concentrations (in ppma) of the clean and cloudy areas of the Ramaura flux-grown ruby, measured by LA-ICP-MS.

	Mg	Cr	Fe	Ni	Ga	La	Pt	Pb
Clean area SP1	5.33	2851	51	2.27	8.83	6.65	1.02	5.58
Clean area SP2	0.83	4706	68	4.20	10.12	0.01	5.10	0.02
Cloudy area SP3	0.65	3153	61	2.03	9.77	55.20	1.04	57.77
Cloudy area SP4	0.74	3287	64	2.15	1.97	74.88	1.09	243.07
Detection limit (ppma)	0.02	0.22	3	0.1	0.01	0.001	0.001	0.001

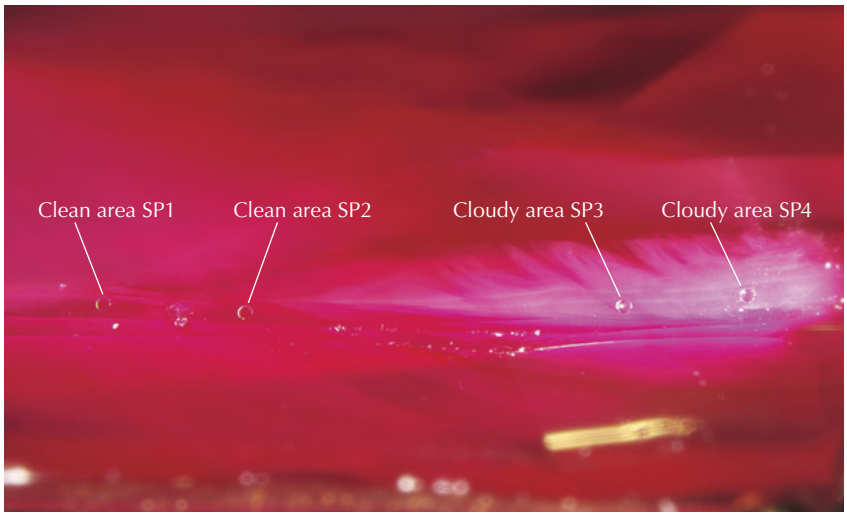

Figure 26. LA-ICP-MS analysis spots located in clean and cloudy regions within the ruby. Field of view 3.99 mm.

within a platinum crucible (Muhlmeister et al., 1998). The La_2O_3 is intentionally added to the flux, and thus the presence of lanthanum is a specific signature of Ramaura synthetic ruby. Most of this stone's inclusions and chemical features supported a synthetic origin, but the natural-looking milky inclusions were unusual and have not been reported until now.

In order to clarify the cause of the natural-looking clouds, LA-ICP-MS results from the clean areas and the cloudy areas reaching the girdle were compared (figure 26). The chemical comparison suggested that the cloudy area was extremely rich in lanthanum and lead relative to the clean area (table 1). How lanthanum and lead are incorporated into this synthetic ruby is not clear, as there were no obvious inclusions that could be tested (such as particles or flakes within the clouds). However, the natural-looking clouds were clearly formed by partial enrichment of lanthanum and lead within this Ramaura synthetic ruby.

Surprisingly, such milky clouds and flux inclusions could be confused with heated natural ruby and might cause misidentification. Careful observation of inclusions in the stone and chemical analysis were both needed to confirm that this was a laboratory-grown ruby.

Makoto Miura

Unique Moiré-Pattern Metallic Inclusion in Paraíba TOURMALINE

The Tokyo laboratory received a 0.33 ct greenish blue oval modified brilliant measuring 5.48 × 3.60 × 2.37 mm (figure 27). Gemological properties, as well as trace element analysis collected with laser ablation–inductively coupled plasma–mass spectrometry (LA-ICP-MS), identified this gem as a Paraíba tourmaline from Brazil.

Microscopic observation revealed planar inclusions consisting of minute particles in the area marked in figure 27. Under fiber-optic illumination, these minute particles had a pink metallic luster. The particles were clustered together, but circular to teardrop-shaped voids in these clusters contained no observable particles (figure 28). Further magnification showed that the particles were arranged in a moiré pattern (figure 29). A moiré pattern occurs when two sets of parallel lines are superimposed, which is sometimes observed in gemstone inclusions (e.g., Fall 2023 *G&G* Micro-World, pp. 375–376). These planar inclusions did not reach the surface of the stone. No fissure was observed along the inclusion. Based on the particles' pinkish color and metallic luster, as well as the stone's high copper content (17095–22700 ppmw), we assume they were native copper. This data was not collected directly from the inclusions but from the girdle of the stone by LA-ICP-MS. Considering the high range of copper concentration compared to the reported copper level of Brazilian Paraíba tourmaline from 119 to 38800 ppmw (Y. Katsurada et al., "Geographic origin determination of Paraíba tourmaline," Winter 2019 *G&G*, pp. 648–659), it is possible they are native copper just

Figure 27. A moiré-pattern metallic inclusion was observed in the marked area of the 0.33 ct Paraíba tourmaline.

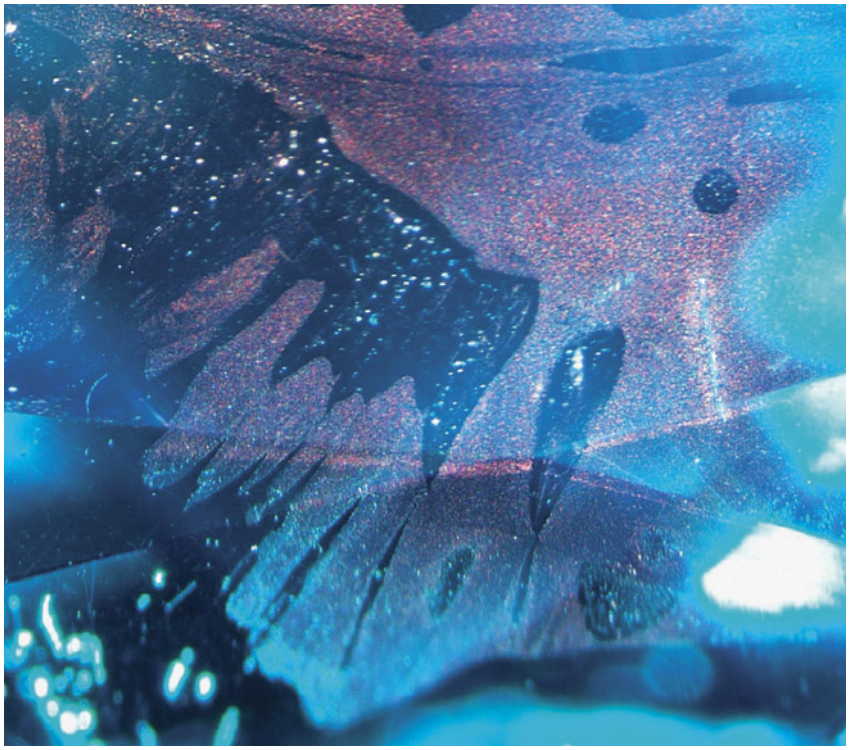

Figure 28. Fiber-optic light showed particles with metallic luster distributed in planar form. Under brightfield or darkfield illumination, the particles' low relief made them almost invisible at first glance. Field of view 1.55 mm.

like the metallic platelets sometimes found in high-copper Paraíba tourmalines (e.g., F. Brandstätter and G. Niedermayr, "Copper and tenorite inclusions in cuprian-elbaite tourmaline from Paraíba, Brazil," Fall 1994 *G&G*, pp. 178–183; Fall 2022 Lab Notes, pp. 362–363; H.A.O. Wang et al., "Further characterisation of native copper inclusions in Cu-bearing tourmaline," *Journal of Gemmology*, Vol. 38, No. 5, 2023, pp. 427–429).

Figure 29. Further magnification revealed the arrangement of particles in a moiré pattern. Field of view 0.93 mm.

Some studies have discussed formation scenarios of dendritic copper inclusions. Brandstätter and Niedermayr (1994) suggested epigenetic exsolution formation because the concentration of CuO decreased toward the native copper inclusions, which were located along the planes corresponding to the trigonal symmetry of tourmaline. On the other hand, Wang et al. (2023) suggested syngenetic formation rather than epigenetic formation, based on the distribution of valence states of copper (metallic copper/Cu^{2+}) and the presence of liquid inclusions similar in shape to dendritic native copper.

The inclusions we observed were different from the dendritic inclusions discussed in previous studies in terms of pattern and orientation in the host tourmaline. Consequently, there could be other mechanisms or scenarios at play with these inclusions, including the possibility of a material other than native copper.

Kanako Otsuka and Yusuke Katsurada

PHOTO CREDITS
Shunsuke Nagai—1; Hikaru Sato—2; Annie Haynes—3; Taryn Linzmeyer—4; Jian Xin (Jae) Liao—7, 12; Courtney Robb—9; Diego Sanchez—10, 11; Gaurav Bera—14, 16, 19, 20, 22, 23A; Andrew Aron—23 (B and C); Lubna Sahani—17; Makoto Miura—25, 26; Shunsuke Nagai—27, 29; Kanako Otsuka—28